

VIMD: Monocular Visual-Inertial Motion and Depth Estimation

Saimouli Katragadda and Guoquan Huang

Abstract— Accurate and efficient dense metric depth estimation is crucial for 3D visual perception in robotics and XR. In this paper, we develop a monocular visual-inertial motion and depth (VIMD) learning framework to estimate dense metric depth by leveraging accurate and efficient MSCKF-based monocular visual-inertial motion tracking. At the core the proposed VIMD is to exploit multi-view information to iteratively refine per-pixel scale, instead of globally fitting an invariant affine model as in the prior work. The VIMD framework is highly modular, making it compatible with a variety of existing depth estimation backbones. We conduct extensive evaluations on the TartanAir and VOID datasets and demonstrate its zero-shot generalization capabilities on the AR Table dataset. Our results show that VIMD achieves exceptional accuracy and robustness, even with extremely sparse points—as few as 10-20 metric depth points per image. This makes the proposed VIMD a practical solution for deployment in resource-constrained settings, while its robust performance and strong generalization capabilities offer significant potential across a wide range of scenarios.

I. INTRODUCTION

For applications like robotics and extended reality (XR), accurate and efficient metric dense depth estimation is critical for 3D visual perception, which is essential for tasks such as obstacle avoidance and motion planning. Monocular methods, which estimate depth from a single RGB image, are particularly appealing because they use a compact, inexpensive, and common camera. However, purely monocular vision suffers from an inherent scale ambiguity: it can capture the relative shape of a scene but cannot determine the true distances to objects. Knowing exactly how far an obstacle is from the camera can be the difference between safe passage and collision. Integrating inertial data can (partially) resolve this ambiguity. As most mobile devices and robots are already equipped with an IMU, visual-inertial odometry (VIO) or SLAM prevails but typically yields only sparse metric depth from a small set of tracked landmarks [1], which alone cannot provide the dense metric depth map required in safety-critical operations.

Although recent advances in monocular depth prediction have achieved high-quality relative depth estimation [3], [4], these methods still lack the ability to produce outputs with absolute metric scale. A common approach assumes an invariant affinity model and aligns the predicted depth to the sparse VIO depth via per-frame least-squares fitting for a global scale and offset (e.g., see [5]). However, as shown in Fig. 1, the fitted scale and offset vary significantly across frames—particularly the offset, which exhibits much

This work was partially supported by the University of Delaware (UD) College of Engineering, and Google ARCore.

¹The authors are with the Robot Perception and Navigation Group (RPNG), University of Delaware, Newark, DE 19716. Email: {saimouli, ghuang}@udel.edu.

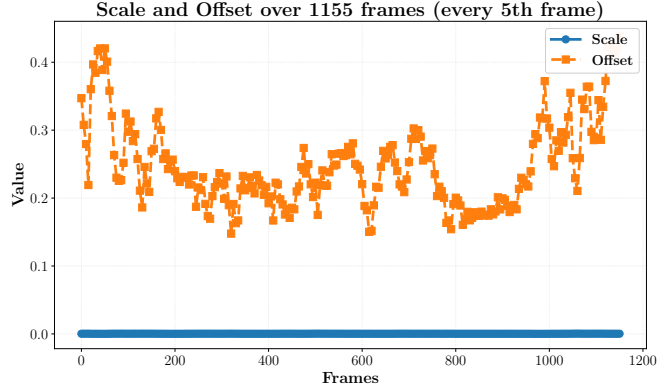


Fig. 1: A motivation result: Invariant affinity is not sufficient to scale monocular depth prediction. Per-frame least-squares fitting of a global scale and offset (every 5th frame) using VOID data [2]. Clearly, the offset varies more than the scale, indicating that a single global affine model cannot reliably align predictions over time.

larger fluctuations than the scale. This temporal instability indicates that the predicted relative depths are not truly affine with respect to the metric depths; that is, they cannot be accurately modeled by a single global scale and offset per frame without unmodeled errors. Besides the unreliable per-frame global fitting, the optimization may become poorly conditioned when sparse points are unevenly distributed or noisy, leading to sensitivity in the fitted parameters and potential error amplification in low-density regions. It has been empirically observed that predicting offset along with scale can hurt depth accuracy [6].

From Fig. 1, it is clear that the offset exhibits much higher variance across frames than the scale, implying that offsets may also vary more significantly across pixels within a single frame (due to factors like viewpoint changes, occlusions, or non-uniform scene structure), thus making them harder to learn reliably at the per-pixel level compared to the more stable scale. Motivated by this observation, we propose to exploit multi-view constraints and learn to optimize iteratively a per-pixel scale, formulated as learning approach that moves beyond the global fitting affine parameters. In particular, the proposed monocular Visual-Inertial Motion and Depth (VIMD) leverages an accurate and efficient MSCKF-based visual-inertial motion estimation module to form multi-view geometric constraints and then refines and predicts dense depth and its uncertainty. As a result, the proposed VIMD improves accuracy and robustness in low-density depth regions. Fig. 2 shows some exemplar performance of the proposed VIMD in both outdoor and indoor scenes, producing high-quality dense metric depths.

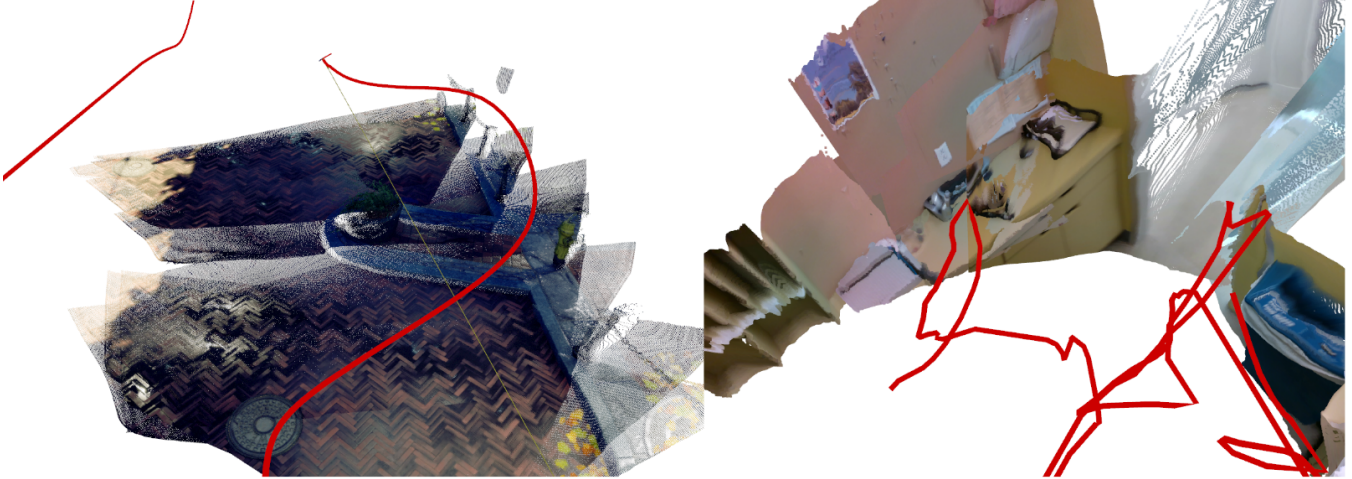


Fig. 2: Overall performance of the proposed VIMD: High-quality dense metric depths in both outdoor and indoor scenes.

II. RELATED WORK

A. Visual-Inertial SLAM and Dense Mapping

While visual-inertial (VI)-SLAM has matured around tightly coupled odometry and optimization backends, most approaches focus on sparse mapping. Kimera [7] augments state estimation with meshing, building per-keyframe meshes via 2D Delaunay triangulation of sparse tracks and fusing them into a global TSDF representation. Similarly, dense aerial mapping in [8] feeds metric VIO poses into a motion-stereo depth module, implicitly transferring the IMU scale into dense maps. Recently, DiT-SLAM [9] integrates visual, inertial, and dense depth constraints in a tightly coupled graph for dense reconstructions. Despite these progresses, dense mapping in SLAM pipelines often show limited generalization.

B. Monocular Scaled Depth Learning

Single-image depth networks such as DPT/MiDaS trained on large-scale, heterogeneous datasets demonstrate strong cross-dataset generalization, but their predictions remain limited to relative (up-to-scale) depth [3], [4], [10]. Self-supervised monocular methods such as Monodepth2 further improve scalability by removing the need for ground-truth labels, yet they still inherit the same scale ambiguity [11]. To mitigate this limitation, efforts have been taken to incorporate additional cues such as inertial or pose information. For instance, in [12] gravity estimated from VIO is used to regularize surface orientation and encourage geometrically consistent predictions. Recently, [13], [14] propose the use of compact scale and offset parameters to represent depth features, reducing the state size of the estimator while improving inertial initialization and overall efficiency.

C. Latent-Code VI-based Dense Depth Estimation

Recent approaches have also integrated dense depth estimation directly into VI estimation pipelines through compact latent codes. For example, CodeVIO [15] introduced a CVAE-based depth decoder whose low-dimensional code is jointly optimized with the VIO state, enabling dense depth with efficient Jacobians and FEJ updates. AB-VINS [16]

pushed this concept further by replacing explicit 3D landmarks with a compressed “AB feature” consisting of a global scale a and bias b , and correction terms, which reduces computational cost while producing dense depth. Similarly, DiT-SLAM [9] uses low-dimensional depth codes coupled with visual-inertial constraints for dense mapping. While effective, these latent-code approaches either constrain depth to low-rank parameterizations or require online optimization of codes, limiting flexibility and generalizability.

D. From Sparse to Dense Depth Completion

Depth completion leverages sparse VIO depth as anchors for dense prediction. VOICED [2] constructs a piecewise-planar scaffold from sparse VIO points and infers dense depth via unsupervised photometric and geometric consistency losses. VI-Depth [6] starts from monocular relative depth, aligns it with sparse VIO depths via a global scale and shift, and then applies a per-pixel refinement network to correct local distortions. This yields metrically accurate dense depth and demonstrates strong cross-dataset generalization, but relies heavily on accurate alignment and struggles with sparse or noisy anchors.

III. LEARNING METRIC DENSE DEPTH

We especially target metrically accurate and robust dense depth in monocular visual-inertial settings and develop an efficient modular visual-inertial motion and depth (VIMD) learning algorithm as depicted in Fig. 3. Unlike latent-code methods such as CodeVIO [17], DiT-SLAM [9], and AB-VINS [16], we do not optimize a compact depth code inside the estimator, avoiding the need for online code optimization and restrictive parameterizations. Instead, we recover per-pixel metric depth by formulating sparse-to-dense alignment as a learning-based optimization problem guided by multi-view geometric constraints from VIO poses. Compared to VI-Depth [6] and VOICED [2], the proposed VIMD fully exploits temporal consistency and multi-view geometry, improving robustness in low-density regions and yielding more reliable depth alongside uncertainty estimates.

In particular, for simplicity, the proposed VIMD pipeline assumes synchronized IMU measurements together with

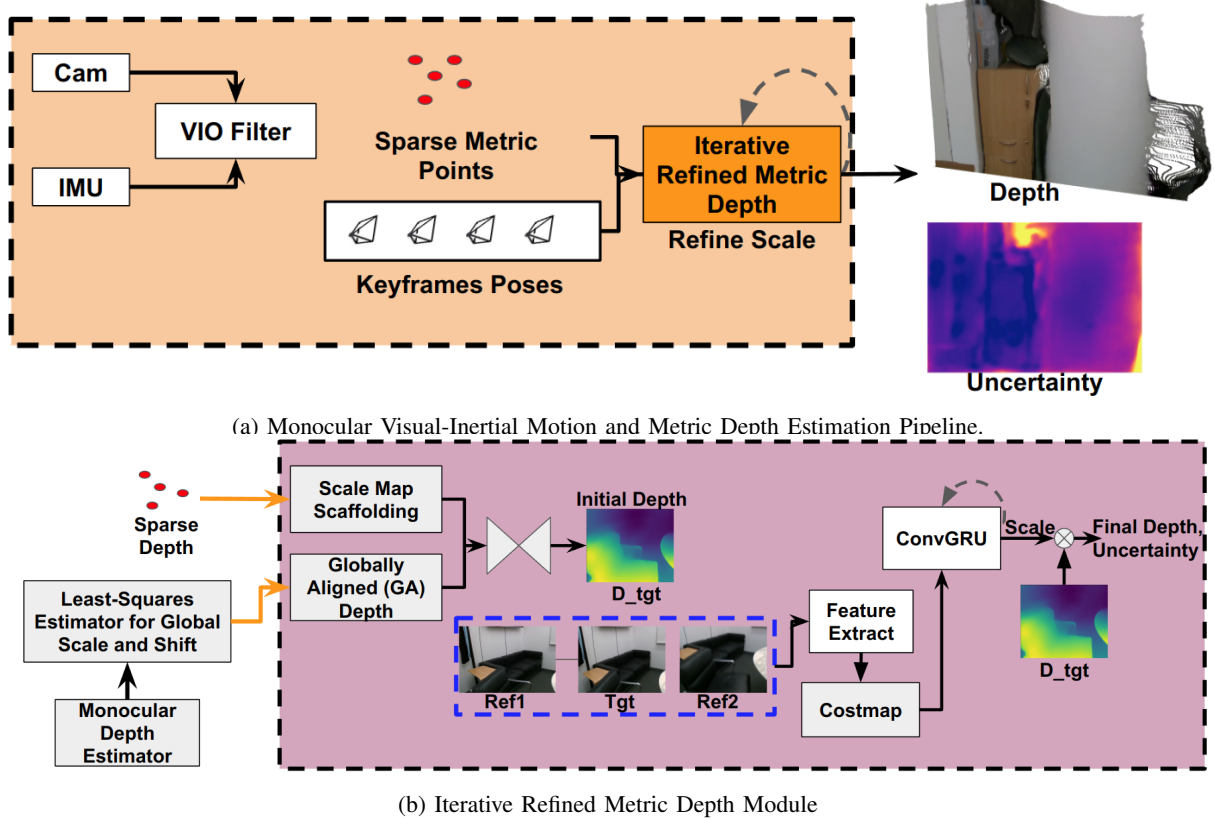


Fig. 3: The proposed visual-inertial motion and depth (VIMD) learning pipeline. (a) System overview: The VIO filter efficiently fuses RGB images and IMU data to estimate sparse features' metric depth and camera poses, which are then passed to the iterative depth refinement module to predict dense metric depth and its uncertainty. (b) Iterative refined metric depth module: The initial metric depth is estimated using the global alignment (GA) depth, which is the metric-aligned depth from the monocular depth estimator, fitted with a global scale and offset via least squares using the sparse depth. Reference frames are warped to the target frame using the predicted depth and VIO poses, and the scale is iteratively refined using a ConvGRU to predict the final depth and uncertainty. Multi-view information is leveraged to improve the accuracy and robustness of depth estimation.

RGB images to estimate camera poses, which however can be easily relaxed by performing online calibration [18]. The inclusion of IMU data in principle enables recovery of the metric scale of monocular vision. Given an image sequence and synchronized IMU measurements, we employ an efficient MSCKF-based [19] VIO module to compute the camera motion and obtain a set of sparse 3D metric points. These metric points are used both to compute a global scale and bias (offset) for depth alignment and to generate a scale-map scaffold for the depth network. The estimated camera poses are also used to enforce the multi-view constraints, thus improving the robustness and accuracy of depth learning.

As the monocular motion estimation module largely leverages the prior VIO work [20], which is briefly described in Appendix I, in the following, we present in detail the design of *Iterative Refined Metric Depth Module* (see Fig. 3b), serving as the key contribution of this paper.

A. Global Alignment

Leveraging the MiDaS DPT-Hybrid network [3], which produces “affine-invariant” inverse depth maps $D_{\text{inv}}(u, v)$,

for all pixels (u, v) , with the corresponding raw depth map $D(u, v) = \frac{1}{D_{\text{inv}}(u, v)}$, we recover the metric scale by a least-squares alignment between the predicted inverse depth and the sparse features' metric depths $1/\|{}^C\mathbf{p}_{f_i}\|$ available from the VIO module (see Appendix I). The aligned inverse depth is modeled with the following affine relationship:

$$Z_{\text{inv}}^{\text{GA}}(u, v) = s_{\text{inv}} D_{\text{inv}}(u, v) + b_{\text{inv}} \quad (1)$$

where s_{inv} and b_{inv} are the global scale and offset, respectively, and obtained from the least-squares fitting.

B. Scale-Map Scaffold

While the previous global alignment corrects the average scale, local residuals may remain inconsistent. Inspired by [6], we construct a spatially varying *scale map scaffold* from the sparse metric points. Let $\mathcal{K} = \{(x_j, y_j)\}_{j=1}^{N_k}$ denote the image coordinates of valid sparse depth samples. At each knot, we compute a local scale factor by comparing the sparse metric inverse depth $Z_{\text{inv}}(x_j, y_j)$ with the network prediction $D_{\text{inv}}(x_j, y_j)$: $\sigma_j = \frac{Z_{\text{inv}}^{\text{GA}}(x_j, y_j)}{D_{\text{inv}}(x_j, y_j)}$. The dense scale map $S(u, v)$ is then obtained by interpolating these knot

values across the image:

$$S(u, v) = \text{Interp}(\mathcal{K}, \{\sigma_j\}, (u, v), \text{linear}) \quad (2)$$

where $\text{Interp}(\cdot)$ denotes 2D scattered linear interpolation. This map serves as a per-pixel prior, normalized to unit range, and is provided as an additional input to the refinement network to guide predictions toward metric depth.

C. Iterative Refinement

Given the globally aligned depth and the scaffold, the refinement network predicts an initial metric depth which is then iteratively corrected using multi-view temporal consistency. Specifically, as shown in Fig. 3b, we refine depth using three frames: one target I_t and two references $\{I_r\}$, with camera intrinsics \mathbf{K} and known VIO poses $\{\bar{q}_k, {}^G\mathbf{p}_{I_k}\}$. Each image is resized to 224×384 for the DPT-Hybrid backbone, which outputs predictions at this resolution. The depth maps are bicubically upsampled to the native resolution $H \times W$, where supervision is applied against full-resolution ground truth, as we found that full-resolution supervision improves scale estimation (see Tab. V). The main steps of this refinement are the following:

1) *Feature extraction*: A lightweight ResNet-18 backbone with stride 4 extracts features $\mathbf{F}_t, \mathbf{F}_r \in \mathbb{R}^{B \times 64 \times H_c \times W_c}$, where $(H_c, W_c) = (H/4, W/4)$. Then a context encoder processes the globally aligned inverse depth $Z_{\text{inv}}^{\text{GA}}$ and the dense scaffold $S(u, v)$, producing a 160-dimensional feature map, which is subsequently divided to form the initial hidden state $\mathbf{h}^{(0)} \in \mathbb{R}^{B \times 128 \times H_c \times W_c}$ and context features $\mathbf{f}_{\text{context}} \in \mathbb{R}^{B \times 32 \times H_c \times W_c}$. A small convolutional head predicts an initial per-pixel scale Δs_{init} and log-variance $\log \sigma_{\text{init}}^2$, yielding the starting inverse depth:

$$Z_{\text{inv}}^{(0)} = Z_{\text{inv}}^{\text{GA}} \odot \Delta s_{\text{init}} \quad (3)$$

2) *Cost computation*: At iteration k , geometric consistency is enforced by warping each reference feature map into the target view using the current depth:

$$\tilde{\mathbf{F}}_{r_i \rightarrow t} = \text{warp}(\mathbf{F}_{r_i}, Z_{\text{inv}}^{(k)}, {}^G\mathbf{p}_{I_t}, {}^G\mathbf{p}_{I_{r_i}}, \mathbf{K}) \quad (4)$$

Cosine similarity with validity masking yields per-reference costs which are then averaged across all references:

$$\mathbf{c}_{r_i} = \left(1 - \langle \text{norm}(\mathbf{F}_t), \text{norm}(\tilde{\mathbf{F}}_{r_i \rightarrow t}) \rangle\right) \odot \mathbf{M}_{r_i} \quad (5)$$

$$\Rightarrow \mathbf{c} = \frac{1}{R} \sum_{i=1}^R \mathbf{c}_{r_i} \quad (6)$$

3) *Projection and recurrent update*: To combine the cost with the current depth hypothesis, we use a projection layer that processes both \mathbf{c} and $Z_{\text{inv}}^{(k)}$ with separate convolutional streams and merges them into a joint representation:

$$\mathbf{p}^{(k)} = \text{Proj}(Z_{\text{inv}}^{(k)}, \mathbf{c}) \in \mathbb{R}^{B \times 32 \times H_c \times W_c} \quad (7)$$

The concatenation of $\mathbf{p}^{(k)}$ and $\mathbf{f}_{\text{context}}$ is fed to a separable ConvGRU with hidden dimension 128. Following [21], [22], gated updates are applied first horizontally (1×5) and then vertically (5×1), yielding

$$\mathbf{h}^{(k+1)} = \text{StepConvGRU}(\mathbf{h}^{(k)}, [\mathbf{p}^{(k)}, \mathbf{f}_{\text{context}}]) \quad (8)$$

from which the network predicts a multiplicative scale correction and log-variance:

$$\Delta s^{(k)} = 1 + 0.5 \tanh(\phi(\mathbf{h}^{(k+1)})) \quad (9)$$

$$\log \sigma^{2(k)} = \psi(\mathbf{h}^{(k+1)}) \quad (10)$$

The inverse depth is then updated and clamped:

$$Z_{\text{inv}}^{(k+1)} = \text{clamp}\left(Z_{\text{inv}}^{(k)} \odot \Delta s^{(k)}, \frac{1}{Z_{\text{max}}}, \frac{1}{Z_{\text{min}}}\right) \quad (11)$$

4) *Final output*: This refinement is repeated for 3 steps, with the cost recomputed at each iteration. The final inverse depth is bicubically upsampled to the native resolution $H \times W$ and output along with the corresponding uncertainty map.

D. Loss Function

Training supervision uses metric ground-truth inverse depth Z_{inv}^* at multiple scales. At scale i , the predicted inverse depth $Z_{\text{inv}}^{[i]}$ is converted to depth $D^{[i]} = 1/Z_{\text{inv}}^{[i]}$ and compared to ground truth $D^* = 1/Z_{\text{inv}}^*$ using an uncertainty-weighted Laplace negative log-likelihood:

$$\mathcal{L}^{[i]} = \frac{|D^{[i]} - D^*|}{b^{[i]}} + \log b^{[i]} \quad (12)$$

$$b^{[i]} = \exp(\log \sigma^{2[i]}) + \epsilon \quad (13)$$

Pixels outside the valid depth range $[D_{\text{min}}, D_{\text{max}}]$ are masked out. In our tests, we set $D_{\text{min}} = 0.1m$ and $D_{\text{max}} = 5m$. The total loss is an exponentially weighted average across all s scales:

$$\mathcal{L}_{\text{depth}} = \frac{\sum_{i=1}^s \gamma^{s-i} \mathcal{L}^{[i]}}{\sum_{i=1}^s \gamma^{s-i}} \quad (14)$$

where $\gamma \in (0, 1)$ controls the relative contribution of coarse and fine scales (for example, we use $\gamma = 0.85$). This formulation encourages both accurate depth prediction and per-pixel uncertainty.

IV. EXPERIMENTAL RESULTS

Our monocular visual-inertial motion estimation module is built on top of OpenVINS [20] (also see Appendix I), while MiDaS DPT Hybrid [3] is used as the depth estimator and ResNet-18 as the backbone network initialized with pretrained ImageNet [23] weights, while the remaining layers are initialized randomly. We employ the AdamW optimizer [24] with $\beta_1 = 0.9$, $\beta_2 = 0.999$, and weight decay $\lambda = 0.001$. The learning rate is set to 10^{-4} for the VOID dataset [2] and 10^{-5} for the TartanAir [25]. A step-based scheduler is used, which halves the learning rate every 8 epochs. Training is performed for 25 epochs on a node with $2 \times$ NVIDIA A4500 GPUs, using a batch size of 8. The entire training process takes approximately 3 days.

We follow the evaluation protocol [6] and consider ground truth depth to be valid between 0.2 and 5 meters. The minimum and maximum depth prediction values in these works are set to 0.1 and 8.0 meters, respectively. We clamp depth predictions, both after global alignment and after applying regressed dense scale maps, to this range. We evaluate in inverse depth space $z = 1/D(u, v)$ (in km^{-1}), which penalizes errors at closer ranges more, with the following metrics: $\text{iMAE} = \frac{1}{M} \sum_i |z_i^{gt} - \hat{z}_i|$, $\text{iRMSE} = \sqrt{\frac{1}{M} \sum_i (z_i^{gt} - \hat{z}_i)^2}$, $\text{iAbsRel} = \frac{1}{M} \sum_i \frac{|z_i^{gt} - \hat{z}_i|}{z_i^{gt}}$, and also compute MAE and RMSE in depth space $\hat{D}(u, v)$ (in mm).

Method	RMSE	MAE	iRMSE	iMAE
GA Only	249.40	169.45	106.17	74.57
VOICED-S* [2]	253.14	131.54	126.30	87.36
KBNet* [26]	263.54	131.54	128.29	66.84
SML* [6]	167.15	97.03	74.67	46.62
Ours	155.23	88.42	67.21	40.18

TABLE I: Quantitative results of evaluation on VOID. All the methods use DPT-H as the depth model and 150 sparse depth points. *Results are taken from the original papers.

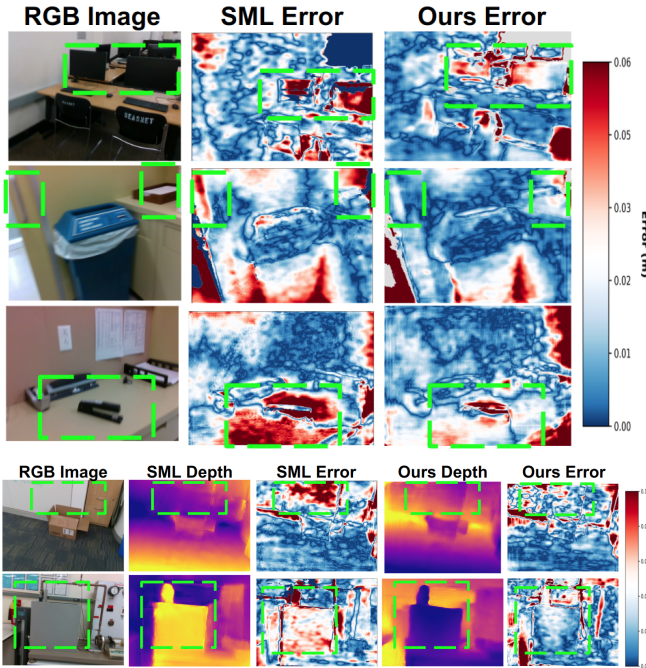


Fig. 4: Qualitative results of evaluation on VOID.

A. Evaluation on VOID

For fair comparison with SOTA methods, we first evaluate our method on the VOID dataset [2], which provides real-world data collected using the Intel RealSense D435i camera and a VIO system. We use 150 samples, consistent with the typical number of observations produced by a lightweight VIO system (120–225 point features under this dataset). We particularly focus on the results against the SML [6], as it was trained on VOID under the same setting. We note that the distribution of sparse points has a significant impact on the network’s performance. Since the point distribution generated by our VIO differs from that of VOID, we ensure fairness by training and evaluating both the SML and our method directly on VOID.

Tab. I shows the quantitative results. Our method achieves iRMSE and iMAE improvements of 37% and 46% respectively with the GA depth, corresponding to relative error reductions of 10% (iRMSE) and 14% (iMAE) compared to the SML. Fig. 4 depicts the qualitative results of depth predictions. Note that error maps are computed against the ground truth depth, where blue indicates low error and red indicates high error. It is clear that as compared to the SML, our method reduces errors particularly in central regions of the depth maps, through iterative scale refinement. Importantly, our predictions are not only metrically more accurate but also produce sharper object boundaries. For

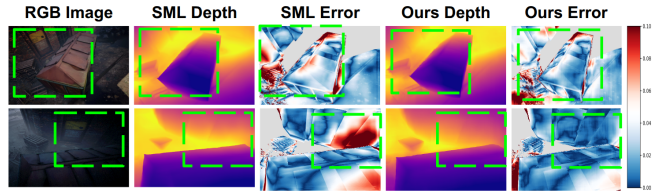


Fig. 5: Qualitative results of evaluation on TartanAir.

instance, in the bottom row of Fig. 4, the vertical pole is reconstructed with reduced error compared to the SML, highlighting the accuracy of our refinement strategy.

More interestingly, beyond absolute accuracy, Tab. II shows the comparative results under different levels of sparse point reduction. Even when the number of points is reduced by 80%, our method consistently outperforms GA and SML across all metrics. Notably, the relative advantage over SML increases as the point density decreases, highlighting the robustness of our approach. This robustness arises from two key factors. First, our method leverages multi-view information through pose integration, which provides additional geometric constraints that compensate for the reduced spatial coverage of sparse points. Second, the ConvGRU module learns to iteratively refine the scale, enabling the network to progressively optimize depth estimates across frames. By combining multi-view cues with recurrent scale refinement, our model is able to maintain both accuracy and stability, even during low density sparse points.

B. Evaluation on TartanAir

To further evaluate the proposed method in large-scale scenarios (where real training data of synchronized RGB-D and IMU is limited), we have leveraged the TartanAir dataset [25], which offers photo-realistic RGB-D sequences generated in diverse simulated environments. We adopt a 70–30 train/test split, sampling sequences from both *easy* and *hard* difficulty levels. Prior to training, we cleaned the data by removing runs with invalid trajectories or corrupted depth maps caused by failures in the rendering front-end. Since the TartanAir does not provide IMU measurements, we generated inertial data by fitting splines (using the `ov_sim` package [20]) to the ground-truth poses and differentiating them to obtain accelerations and angular velocities at 200 Hz. The simulated IMU follows realistic noise characteristics, with an accelerometer noise density of $2.0 \times 10^{-3} \text{ m/s}^2/\sqrt{\text{Hz}}$, an accelerometer random walk of $3.0 \times 10^{-3} \text{ m/s}^3/\sqrt{\text{Hz}}$, a gyroscope noise density of $1.6968 \times 10^{-4} \text{ rad/s}/\sqrt{\text{Hz}}$, and a gyroscope random walk of $1.9393 \times 10^{-5} \text{ rad/s}^2/\sqrt{\text{Hz}}$. Using these simulated IMU signals, we ran the OpenVINS [20] on the TartanAir sequences. Spline interpolation was applied to synchronize visual and inertial streams, and we collected sparse depth points (from MSCKF and SLAM features) along with camera poses. This resulted in a dataset of images, sparse depths, poses that closely reflect the outputs of a real-world visual-inertial motion estimation system. The distribution of sparse depth points in TartanAir differs from that of VOID. Consequently, the pretrained network from [6] fails to generalize when applied directly to our collected data. For a fair comparison, we implemented the training pipeline

Reduction %	RMSE			MAE			iRMSE			iMAE		
	GA	SML	Ours	GA	SML	Ours	GA	SML	Ours	GA	SML	Ours
10	249.65	169.23	158.74	169.51	97.03	89.52	106.27	75.62	69.19	74.61	45.09	41.08
50	251.71	180.26	169.87	171.28	104.07	96.57	107.00	80.24	74.95	75.35	48.38	44.57
80	255.53	216.55	194.88	174.14	129.83	112.47	108.96	98.61	94.47	76.63	60.63	53.17

TABLE II: Performance with respect to different levels of sparse depth reduction.

Method	RMSE	MAE	iRMSE	iMAE	Size(MB)	Time(ms)
GA Only	231.86	231.86	31.68	21.81	—	—
SML [6]	180.53	110.33	27.61	17.24	21.3	15.3
Ours	172.81	103.92	25.70	15.72	15.1	19.6

TABLE III: Qualitative results of evaluation on TartanAir v1.

for the baseline method and retrained it on the processed TartanAir dataset alongside the proposed approach.

Fig. 5 shows qualitative results and Tab. III reports the quantitative results on TartanAir. As evident, our method achieves the lowest error across all metrics, outperforming the SML [6] by 4.3% in RMSE, 5.8% in MAE, 6.9% in iRMSE, and 8.8% in iMAE. Beyond accuracy, our model is more compact, with a size of 15.1 MB compared to 21.3 MB for the SML. In terms of runtime, our method achieves 19.6 ms per frame on an NVIDIA RTX 2080Ti GPU, while the SML runs slightly faster at 15.3 ms. This additional overhead primarily comes from the GRU refinement module, which can be further optimized through TensorRT [27]. These results highlight the benefit of incorporating pose-based multi-view constraints and iterative scale refinement into the depth prediction pipeline. By leveraging both sparse points and temporal consistency, our method not only improves predictive accuracy but reduces model complexity, making it more practical for deployment in resource-constrained settings.

C. Evaluation on AR Table

To evaluate the generalization ability of our model, we trained exclusively on TartanAir and then performed *zero-shot* deployment on the AR Table dataset [28]. The AR Table sequences consist of real-world RGB-D+IMU data stored in rosbags. For evaluation, we used a minute of data and filtered out outlier sparse depths with errors greater than 8 cm. Quantitative results are summarized in Tab. IV. Across both Table 1 and Table 2 sequences, our method consistently outperforms the GA-only baseline and the SML approach. Without iterative refinement (0 iter), our method already achieves competitive accuracy, reducing both RMSE and MAE relative to SML. When iterative refinement is enabled (3 iters), errors decrease further: on Table 1, RMSE improves from 547.63 to 541.02, while AbsRel is reduced from 0.120 to 0.117. On Table 2, RMSE decreases from 368.10 to 357.47 and AbsRel from 0.131 to 0.111. These results highlight that iterative scale and geometry refinement aids to further reduce the depth error.

Importantly, this zero-shot experiment demonstrates that our method generalizes effectively to real-world datasets despite training in simulated drone environments (TartanAir). The improvements obtained through iterative refinement indicate that the model is capable of leveraging underlying

Dataset	Method	RMSE	MAE	AbsRel
Table 1	GA	657.23	459.52	0.391
	SML	563.47	334.84	0.121
	Ours (0 iter)	547.63	330.10	0.120
	Ours (3 iter)	541.02	326.97	0.117
Table 2	GA	626.71	251.98	0.140
	SML	387.08	186.43	0.116
	Ours (0 iter)	368.10	192.34	0.131
	Ours (3 iter)	357.47	185.54	0.111

TABLE IV: Evaluation results on the AR Table datasets.

geometric cues at test time, which is crucial for practical deployment in diverse environments where the training and deployment domains may differ significantly.

D. Ablation Study

We have further conducted an ablation study on the VOID-150 dataset to understand the contribution of different components in the proposed VIMD model. Tab. V summarizes the results. The first factor examined is prediction resolution. Training with only low-resolution L1 supervision produces the largest error, consistent with prior findings in [6]. This outcome suggests that restricting supervision to a coarse scale limits the network’s ability to recover fine structural details. When full-resolution supervision is introduced by bilinearly up-sampling predictions before supervision, the error decreases noticeably. Our conjecture is that the additional pixel-level guidance forces the network to preserve object boundaries and local depth gradients, which are otherwise smoothed out at lower resolutions.

We then study the effect of recurrent refinement with ConvGRU. Adding this module consistently improves all metrics, with the most significant gains in iRMSE and iMAE. Unlike static single-pass prediction, the recurrent updates allow the network to iteratively align depth estimates across frames while correcting the global scale. We hypothesize that this iterative mechanism encourages the network to exploit multi-view consistency: features that remain stable across frames are reinforced, while transient ambiguities are suppressed. This explains why improvements are particularly strong in inverse-error metrics, which are sensitive to structural misalignment at different depth ranges.

We finally investigate uncertainty modeling. Replacing the L1 loss with a Laplace negative log-likelihood not only lowers the overall error but also sharpens predictions in ambiguous regions. We attribute this to the model’s ability to down-weight supervision in areas where sparse depth samples are noisy or inconsistent, allowing it to focus learning on more reliable cues. In contrast, using a Gaussian likelihood did not converge reliably—likely due to the heavier tails of depth errors in real-world sparse inputs, which are better captured by a Laplace distribution.

Loss Used	Lower is better ↓				Ablation switches		
	RMSE	MAE	iRMSE	iMAE	Full-res	GRU Refinement	Uncert.
L1	167.15	95.69	75.42	44.69	✗	✗	✗
L1	163.70	91.18	71.14	41.17	✓	✗	✗
L1	155.23	88.42	67.21	40.18	✓	✓	✗
Laplace	158.41	86.72	66.48	38.22	✓	✓	✓
Gaussian	-	-	-	-	✓	✗	✓

TABLE V: Ablation study of the proposed VIMD on the VOID-150 dataset. “Full-res” means the depth prediction (144×284) is bilinearly up-sampled to 480×640 and supervised at native resolution. “Warp” enables ConvGRU multi-view warping. “Uncert.” indicates the Laplace negative-log-likelihood head is used instead of pure L1.

Together, these results show that each component tackles a distinct failure mode: full-resolution supervision reduces over-smoothing, the ConvGRU refinement mitigates scale drift while enforcing temporal consistency, and uncertainty modeling enhances robustness to noisy supervision. The combination of all three produces the most accurate and stable predictions compared to other state-of-the-art methods.

V. CONCLUSIONS AND FUTURE WORK

In this paper, we have developed a novel monocular visual-inertial motion and depth (VIMD) model to learn dense metric depth from the minimal sensing platform of a monocular camera and IMU. At the core of our approach is to exploit multi-view information within a learning-based framework to iteratively optimize per-pixel scale. Additionally, the prediction of uncertainty yields more reliable depth for downstream applications and supervision at full image resolution enhances scale accuracy. As a result, the proposed VIMD model is robust in scenarios with sparse features and demonstrates generalization ability, including zero-shot performance on real-world datasets.

Nevertheless, we did observe that the cost-geometry optimization remains sensitive to textureless regions and pose drift, which can limit performance in challenging environments. Therefore, for future work, we will extend this model into a full-fledged efficient SLAM by training in an end-to-end fashion that jointly optimizes both pose and scale. Note that the proposed VIMD model can be used as a prior to Gaussian-Splatting (GS)-SLAM [29] for monocular language photorealistic mapping.

APPENDIX I VISUAL-INERTIAL MOTION ESTIMATION

The visual-inertial motion estimation module in the proposed VIMD pipeline (see Fig. 3) is built on top of the monocular MSCKF-VIO (i.e., OpenVINS [20]), which offers accurate and efficient ego-motion estimates by fusing IMU data and visual measurements of sparse point features and is briefly described in the following. In particular, at time t_k , the system state \mathbf{x}_k consists of the current navigation states \mathbf{x}_{I_k} , historical IMU pose clones \mathbf{x}_C , and a subset of 3D environmental (SLAM) point features, \mathbf{x}_f :

$$\mathbf{x}_k = [\mathbf{x}_{I_k}^\top \mathbf{x}_C^\top \mathbf{x}_f^\top]^\top, \quad \mathbf{x}_C = [\mathbf{x}_{T_k}^\top \dots \mathbf{x}_{T_{k-c}}^\top]^\top \quad (15)$$

$$\mathbf{x}_{I_k} = [{}^I_G \bar{q}^\top \ {}^G \mathbf{p}_{I_k}^\top \ {}^G \mathbf{v}_{I_k}^\top \ \mathbf{b}_g^\top \ \mathbf{b}_a^\top]^\top \quad (16)$$

$$\mathbf{x}_f = [{}^G \mathbf{p}_{f_1}^\top \dots {}^G \mathbf{p}_{f_g}^\top]^\top \quad (17)$$

where ${}^I_G \bar{q}$ is the unit quaternion (${}^I_G \mathbf{R}$ in rotation matrix form) that represents the rotation from the global $\{G\}$ to the IMU frame $\{I\}$; ${}^G \mathbf{p}_I$, ${}^G \mathbf{v}_I$, and ${}^G \mathbf{p}_{f_i}$ are the IMU position, velocity, and i 'th point feature position in $\{G\}$; \mathbf{b}_g and \mathbf{b}_a are the gyroscope and accelerometer biases; $\mathbf{x}_{T_i} = [{}^I_G \bar{q}^\top \ {}^G \mathbf{p}_{T_i}^\top]^\top$.

A. IMU Propagation

The inertial kinematics are used to evolve the state from time t_k to t_{k+1} [30], [31]:

$$\mathbf{x}_{I_{k+1}} = \mathbf{f}(\mathbf{x}_{I_k}, \mathbf{a}_{m_k}, \boldsymbol{\omega}_{m_k}) \quad (18)$$

where the linear acceleration \mathbf{a}_{m_k} and the angular velocity $\boldsymbol{\omega}_{m_k}$ measurements are contaminated by zero-mean white Gaussian noises. The MSCKF linearizes this nonlinear model and propagates the state estimate and covariance [19].

B. Visual Update

The monocular camera provides bearing observations to sparse point features in the environment. These visual measurements are used to update the motion states with the following measurement function (note that we here assume the global 3D feature model [20]):

$$\mathbf{z}_k = \mathbf{h}(\mathbf{x}_k) + \mathbf{n}_k =: \Lambda({}^C_k \mathbf{p}_f) + \mathbf{n}_k \quad (19)$$

$${}^C_k \mathbf{p}_f = [x \ y \ z]^\top = {}^I_G \mathbf{R} {}^I_k \mathbf{R} ({}^G \mathbf{p}_f - {}^G \mathbf{p}_{I_k}) + {}^C \mathbf{p}_I \quad (20)$$

$$\Lambda([x \ y \ z]^\top) =: [x/z \ y/z]^\top \quad (21)$$

where \mathbf{n}_k is the white Gaussian bearing measurement noise and $\{{}^I_G \mathbf{R}, {}^C \mathbf{p}_I\}$ is the known camera-IMU rigid transformation. Linearizing (19) yields the following residual:

$$\tilde{\mathbf{z}}_k \simeq \mathbf{H}_k \tilde{\mathbf{x}}_k + \mathbf{n}_k = \mathbf{H}_{T_k} \tilde{\mathbf{x}}_{T_k} + \mathbf{H}_{f_k} {}^G \tilde{\mathbf{p}}_f + \mathbf{n}_k \quad (22)$$

where \mathbf{H}_{T_k} and \mathbf{H}_{f_k} are the measurement Jacobians in respect to the observing pose $\hat{\mathbf{x}}_{T_k}$ and 3D point feature ${}^G \tilde{\mathbf{p}}_f$. We stack the measurements from different times and have:

$$\tilde{\mathbf{z}}_c = \mathbf{H}_T^c \tilde{\mathbf{x}}_C + \mathbf{H}_f^c {}^G \tilde{\mathbf{p}}_f + \mathbf{n}_c \quad (23)$$

where $\tilde{\mathbf{z}}_c$ is the stacked measurement residual; \mathbf{H}_T^c and \mathbf{H}_f^c are the stacked Jacobians; $\mathbf{n}_c \sim \mathcal{N}(\mathbf{0}, \mathbf{R}_c)$ is the stacked measurement noise (normally 1 pixel). We then perform EKF update with two types of point features: (i) *SLAM Point*: The state \mathbf{x}_f contains ${}^G \mathbf{p}_f$, thus (23) can directly update the state using the standard EKF equations. (ii) *MSCKF Point*: For features that are not in the state, we project (23) onto the left nullspace of \mathbf{H}_f^c (i.e., $\mathbf{N}_f^\top \mathbf{H}_f^c = \mathbf{0}$), and construct the following residual independent of ${}^G \tilde{\mathbf{p}}_f$ for update [19]:

$$\mathbf{N}_f^\top \tilde{\mathbf{z}}_c = \mathbf{N}_f^\top \mathbf{H}_T^c \tilde{\mathbf{x}}_C + \mathbf{N}_f^\top \mathbf{H}_f^c {}^G \tilde{\mathbf{p}}_f + \mathbf{N}_f^\top \mathbf{n}_c \quad (24)$$

$$\Rightarrow \tilde{\mathbf{z}}'_c = \mathbf{H}_T' \tilde{\mathbf{x}}_C + \mathbf{n}' \quad (25)$$

REFERENCES

[1] G. Huang, “Visual-inertial navigation: A concise review,” in *Proc. International Conference on Robotics and Automation*, Montreal, Canada, May 2019.

[2] A. Wong, X. Fei, S. Tsuei, and S. Soatto, “Unsupervised depth completion from visual inertial odometry,” *IEEE Robotics and Automation Letters*, vol. 5, no. 2, pp. 1899–1906, 2020.

[3] R. Ranftl, A. Bochkovskiy, and V. Koltun, “Vision transformers for dense prediction,” *ICCV*, 2021.

[4] R. Birk, D. Wofk, and M. Müller, “Midas v3.1 – a model zoo for robust monocular relative depth estimation,” *arXiv preprint arXiv:2307.14460*, 2023.

[5] N. Merrill, P. Geneva, S. Katragadda, C. Chen, and G. Huang, “Fast monocular visual-inertial initialization leveraging learned single-view depth,” in *Proc. Robotics: Science and Systems (RSS)*, Daegu, Republic of Korea, July 2023.

[6] D. Wofk, R. Ranftl, M. Müller, and V. Koltun, “Monocular visual-inertial depth estimation,” in *2023 IEEE International Conference on Robotics and Automation (ICRA)*. IEEE, 2023, pp. 6095–6101.

[7] A. Rosinol, M. Abate, Y. Chang, and L. Carlone, “Kimera: an open-source library for real-time metric-semantic localization and mapping,” in *IEEE Intl. Conf. on Robotics and Automation (ICRA)*, 2020. [Online]. Available: <https://github.com/MIT-SPARK/Kimera>

[8] Z. Yang, F. Gao, and S. Shen, “Real-time monocular dense mapping on aerial robots using visual-inertial fusion,” in *2017 IEEE International Conference on Robotics and Automation (ICRA)*. IEEE, 2017, pp. 4552–4559.

[9] M. Zhao, D. Zhou, X. Song, X. Chen, and L. Zhang, “Dit-slam: real-time dense visual-inertial slam with implicit depth representation and tightly-coupled graph optimization,” *Sensors*, vol. 22, no. 9, p. 3389, 2022.

[10] S. F. Bhat, R. Birk, D. Wofk, P. Wonka, and M. Müller, “Zoedepth: Zero-shot transfer by combining relative and metric depth,” *arXiv preprint arXiv:2302.12288*, 2023.

[11] C. Godard, O. Mac Aodha, M. Firman, and G. J. Brostow, “Digg into self-supervised monocular depth prediction,” October 2019.

[12] X. Fei, A. Wong, and S. Soatto, “Geo-supervised visual depth prediction,” *IEEE Robotics and Automation Letters*, vol. 4, no. 2, pp. 1661–1668, 2019.

[13] “Fast monocular visual-inertial initialization leveraging learned single-view depth,” *Robotics: Science and Systems (RSS)* 2023, 2023.

[14] N. Merrill, P. Geneva, S. Katragadda, C. Chen, and G. Huang, “Fast and robust learned single-view depth-aided monocular visual-inertial initialization,” *The International Journal of Robotics Research*, p. 02783649241262452.

[15] X. Zuo, N. Merrill, W. Li, Y. Liu, M. Pollefeys, and G. Huang, “Codevio: Visual-inertial odometry with learned optimizable dense depth,” in *2021 ieee international conference on robotics and automation (icra)*. IEEE, 2021, pp. 14 382–14 388.

[16] N. Merrill and G. Huang, “Visual-inertial slam as simple as a, b, vins,” *arXiv preprint arXiv:2406.05969*, 2024.

[17] X. Zuo, N. Merrill, W. Li, Y. Liu, M. Pollefeys, and G. Huang, “Codevio: Visual-inertial odometry with learned optimizable dense depth,” in *Proc. of the IEEE International Conference on Robotics and Automation*, Xi'an, China, 2021.

[18] Y. Yang, P. Geneva, X. Zuo, and G. Huang, “Online self-calibration for visual-inertial navigation systems: Models, analysis and degeneracy,” *IEEE Transactions on Robotics*, May 2023.

[19] A. I. Mourikis and S. I. Roumeliotis, “A multi-state constraint kalman filter for vision-aided inertial navigation,” in *Proceedings 2007 IEEE international conference on robotics and automation*. IEEE, 2007, pp. 3565–3572.

[20] P. Geneva, K. Eckenhoff, W. Lee, Y. Yang, and G. Huang, “OpenVINS: a research platform for visual-inertial estimation,” in *Proc. of the IEEE International Conference on Robotics and Automation*, Paris, France, 2020. [Online]. Available: https://github.com/rpng/open_vins

[21] Z. Teed and J. Deng, “Raft: Recurrent all-pairs field transforms for optical flow,” in *European conference on computer vision*. Springer, 2020, pp. 402–419.

[22] X. Gu, W. Yuan, Z. Dai, S. Zhu, C. Tang, Z. Dong, and P. Tan, “Dro: Deep recurrent optimizer for video to depth,” *IEEE Robotics and Automation Letters*, vol. 8, no. 5, pp. 2844–2851, 2023.

[23] J. Deng, W. Dong, R. Socher, L.-J. Li, K. Li, and L. Fei-Fei, “Imagenet: A large-scale hierarchical image database,” in *2009 IEEE conference on computer vision and pattern recognition*. Ieee, 2009, pp. 248–255.

[24] I. Loshchilov and F. Hutter, “Decoupled weight decay regularization,” in *International Conference on Learning Representations*.

[25] W. Wang, D. Zhu, X. Wang, Y. Hu, Y. Qiu, C. Wang, Y. Hu, A. Kapoor, and S. Scherer, “Tartanair: A dataset to push the limits of visual slam,” in *2020 IEEE/RSJ International Conference on Intelligent Robots and Systems (IROS)*. IEEE, 2020, pp. 4909–4916.

[26] A. Wong and S. Soatto, “Unsupervised depth completion with calibrated backprojection layers,” in *Proceedings of the IEEE/CVF International Conference on Computer Vision*, 2021, pp. 12 747–12 756.

[27] NVIDIA TensorRT, NVIDIA Corporation, 2025, high-performance deep learning inference SDK. [Online]. Available: <https://developer.nvidia.com/tensorrt>

[28] C. Chen, P. Geneva, Y. Peng, W. Lee, and G. Huang, “Monocular visual-inertial odometry with planar regulararitie,” in *Proc. of the IEEE International Conference on Robotics and Automation*, London, UK, 2023.

[29] S. Katragadda, C.-Y. Wu, Y. Guo, X. Huang, G. Huang, and L. Ren, “Online language splatting,” in *International Conference on Computer Vision (ICCV)*, 2025. [Online]. Available: <https://arxiv.org/abs/2503.09447>

[30] A. B. Chatfield, *Fundamentals of High Accuracy Inertial Navigation*. Reston, VA: American Institute of Aeronautics and Astronautics, Inc., 1997.

[31] N. Trawny and S. I. Roumeliotis, “Indirect Kalman filter for 3D attitude estimation,” University of Minnesota, Dept. of Comp. Sci. & Eng., Tech. Rep., Mar. 2005.